Raman solitons in waveguides with simultaneous quadratic and Kerr nonlinearities

William R. Rowe ⬤, Dmitry V. Skryabin ⬤, and Andrey V. Gorbach ⬤*

Centre for Photonics and Photonic Materials, Department of Physics, University of Bath, Bath BA2 7AY, United Kingdom

We analyze Raman-induced self-frequency shift in two-component solitons supported by both quadratic and cubic nonlinearities. Treating Raman terms as a perturbation, we derive expressions for soliton velocity and frequency shifts of the fundamental frequency and second-harmonic soliton components. We find these predictions compare well with simulations of soliton propagation. We also show that Raman shift can cause two-component solitons to approach the boundary of their own existence and subsequently trigger soliton instabilities. In some cases these instabilities are accompanied by an almost complete transfer of power to the second harmonic and emergence of a single-component Kerr solitonic pulse.

I. INTRODUCTION

Intrapulse Raman scattering (IRS) arises in ultrashort pulses with sufficient spectral breadth, allowing stimulated Raman scattering between frequencies within the pulse [1]. IRS in the regime of soliton propagation in materials with Kerr nonlinearity is known to lead to the continuous downshift of the central soliton frequency. This phenomenon is commonly referred to as the soliton self-frequency shift (SFS) [1–3]. In systems with cubic ($\chi^{(3)}$) nonlinearity SFS can be described using a perturbation expansion as an adiabatic transformation of soliton frequency and velocity [4,5]. This description has been crucial in the explanation of supercontinuum generation in optical fibers [6–8] and has been shown to work well even in cases of strong Raman response, for example, in air-core fibers [9].

Nonlinear pulse dynamics in systems with quadratic ($\chi^{(2)}$) and $\chi^{(3)}$ nonlinearity have become the subject of research recently, in particular prompted by the emergence of lithium niobate (LiNbO$_3$, or LN) on insulator waveguides [10–12]. These waveguides are an exciting new platform for nonlinear optics [13,14]. They combine the broadband transparency and high quadratic ($\chi^{(2)}$) nonlinearity of LN with the dispersion engineering of high-index-contrast nanowaveguides [13,14]. Together these aspects allow for generation, at experimentally achievable powers, of two-component temporal solitons [15]. Two-component solitons, sometimes called two-color solitons, are solitonic excitations consisting of two pulses, one at a fundamental frequency (FF) and one at its second harmonic (SH), locked together as they propagate [16]. This requirement that both components propagate together with the same group velocity means that two-component solitons are inherently more fragile than their Kerr counterparts [15,16]. However, they can be excited under normal dispersion, meaning two-component solitons may exist across the spectral range that does not allow bright Kerr solitons [15,16]. Two-component solitons have been studied extensively in both $\chi^{(2)}$-only and $\chi^{(2)} + \chi^{(3)}$ systems [16–19].

LN is known to have a strong Raman response [20], and recent studies into LN nano-waveguides suggest the existence of two-component Raman solitons [10–12]. So far, however, no theory has been developed for IRS in such systems. It is therefore the purpose of this work to analyze two-component Raman solitons, using LN nanowaveguides as an illustrative example. In particular we would like to explore whether the delicate balance between the two components with their different dispersions can be preserved when accounting for the effects of Raman scattering.

II. MODEL

We consider a waveguide with a fixed cross section in the x-y plane perpendicular to the direction of propagation z. The FF and SH fields are expressed as $A_f \exp(i\beta_f z - i\omega_f t)$ and $A_s \exp(i\beta_s z - i\omega_s t)$, respectively. Here, $\omega_s = 2\omega_f$, A_f and A_s are the field envelopes, t is time, and z is distance along the waveguide. $|A_{f,s}|^2$ are scaled to be measured in watts. β_f and β_s are the propagation constants, defined as

$$\beta_k(\omega) = \sum_{m=0} \frac{[\omega - \omega_k]^m}{m!} \beta_{km}, \qquad \beta_{km} = \left.\frac{\partial^m \beta_k}{\partial \omega^m}\right|_{\omega_k}, \quad (1)$$

where k is either f or s, denoting the FF or SH, respectively.

We normalize these fields by defining the dispersion length of the FF component, $z_d = 2t_0^2/|\beta_{f2}|$, where t_0 is a characteristic timescale, typically, the FF pulse width. Our amplitudes therefore become the normalized envelope functions, $U_f = \sqrt{2}\rho_2 z_d A_f$ and $U_s = \rho_2 z_d A_s$. ρ_2 is the effective $\chi^{(2)}$ nonlinearity coupling the two modes, which we define later. Propagating along the waveguide, these field envelopes evolve

---

as

$$
i\partial_\xi U_f + r_2\partial_\tau^2 U_f + U_f^* U_s e^{i\kappa\xi}
$$
$$
+ U_f[\alpha_f|U_f|^2 + \alpha_c|U_s|^2] = \varepsilon_f(U_f, U_s),
$$

$$
i\partial_\xi U_s + is_1\partial_\tau U_s + s_2\partial_\tau^2 U_s + \frac{U_f^2}{2}e^{-i\kappa\xi}
$$
$$
+ U_s[\alpha_s|U_s|^2 + \alpha_c|U_f|^2] = \varepsilon_s(U_f, U_s), \quad (2)
$$

where we have defined the normalized coordinates $\xi = z/z_d$ in the direction of propagation and $\tau = [t - \beta_{f1}z]/t_0$, the transverse time coordinate moving with the group velocity of the fundamental field. We assume that dispersion of third order and higher is negligible, but the effects of including these terms are known in the absence of Raman scattering [15].

We define the normalized dispersion parameters

$$
r_2 = -\frac{z_d}{2t_0^2}\beta_{f2}, \qquad s_2 = -\frac{z_d}{2t_0^2}\beta_{s2}, \quad (3)
$$

the walk-off parameter $s_1 = [\beta_{s1} - \beta_{f1}]z_d/t_0$, and the phase-mismatch parameter $\kappa = [\beta_s(\omega_s) - 2\beta_f(\omega_f)]z_d$. The coefficients α_k are defined by the balance between the effective $\chi^{(3)}$ and $\chi^{(2)}$ nonlinearities and dispersion length z_d, with

$$
\alpha_f = \frac{3\rho_{3,f}}{2\rho_2^2 z_d}, \quad \alpha_s = \frac{3\rho_{3,s}}{\rho_2^2 z_d}, \quad \alpha_c = \frac{3\rho_{3,c}}{\rho_2^2 z_d}. \quad (4)
$$

$\rho_{3,f}$, $\rho_{3,s}$, and $\rho_{3,c}$ are the effective $\chi^{(3)}$ nonlinearities in the FF mode, in the SH mode, and between the two modes, respectively. We note that $\alpha_{f,s,c}$ are set both by the waveguide geometry via ρ_2 and $\rho_{3,f,s,c}$ and by the input pulse parameters through t_0 via z_d. Effective nonlinearities are calculated taking overlap integrals of the appropriate spatial mode profiles with the nonlinear material [21,22],

$$
\rho_2 = \frac{\varepsilon_0\omega_f}{4N_f\sqrt{N_s}}\int \vec{e}_s \cdot \hat{\chi}^{(2)}\!:\!\vec{e}_f^2 d\Omega,
$$
$$
\gamma_{kjpl} = \frac{\epsilon_0\omega_k}{16\sqrt{N_kN_jN_pN_l}}\int \vec{e}_k^* \cdot \hat{\chi}^{(3)}\!:\!\vec{e}_j^*\vec{e}_p\vec{e}_l d\Omega,
$$

$$(5)$$

where electric-field profiles of the FF and SH modes are $\vec{e}_f$ and $\vec{e}_s$, respectively. N_k is the normalization factor for mode k. $\hat{\chi}^{(2)}$ and $\hat{\chi}^{(3)}$ are the material $\chi^{(2)}$ and $\chi^{(3)}$ nonlinear tensors, respectively, and Ω is the cross-sectional area of the nonlinear material in the waveguide. $\rho_{3,f} = \gamma_{ffff}$, $\rho_{3,s} = \gamma_{ssss}$, and $\rho_{3,c} = 2\gamma_{fssf} = \gamma_{sffs}$.

On the right-hand side of Eq. (2) we have additional terms, ε_f and ε_s, which must be zero for perfect soliton solutions to exist in the system (see Sec. III). We use these terms to include the delayed Raman response in our model by setting

$$
\varepsilon_f(U_f, U_s) = f_R U_f \int_{-\infty}^{\infty} [\delta(\tau' - \tau) - R(\tau' - \tau)]
$$
$$
\times [\alpha_f|U_f(\tau')|^2 + \alpha_c|U_s(\tau')|^2]d\tau',
$$

$$
\varepsilon_s(U_f, U_s) = f_R U_s \int_{-\infty}^{\infty} [\delta(\tau' - \tau) - R(\tau' - \tau)]
$$
$$
\times [\alpha_s|U_s(\tau')|^2 + \alpha_c|U_f(\tau')|^2]d\tau', \quad (6)
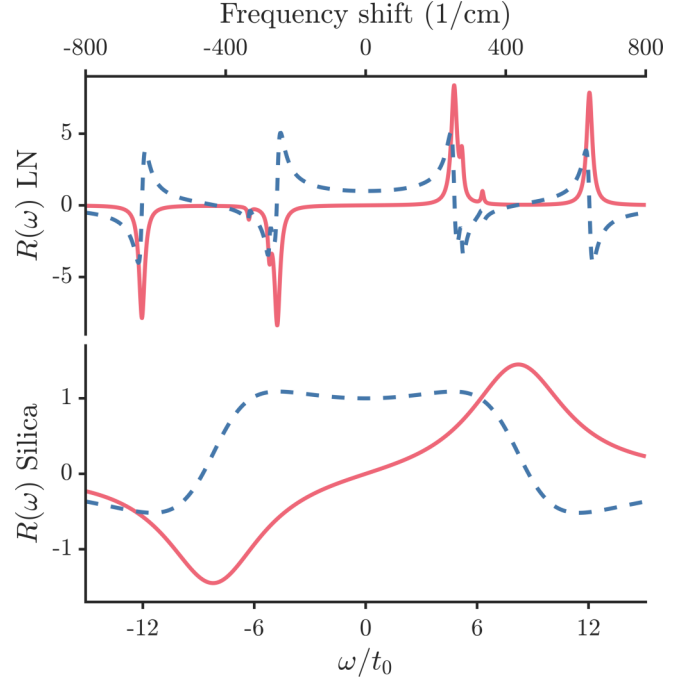$$

FIG. 1. Real (dashed blue line) and imaginary (solid red line) parts of the Raman response spectra $R(\omega)$ for LN (top) and silica (bottom).

where $\delta(\tau)$ is the Dirac delta function and f_R is the fraction of the total material $\chi^{(3)}$ response that is attributed to delayed Raman response, where for LN we use $f_R = 0.5$ [12,20]. For silica the Raman fraction is known to be $f_R = 0.18$ [8]. The Raman response function of the nonlinear material

$$
R(\tau) = \Theta(\tau)\sum_{n=1}^{N} f_n\frac{\tau_{1,n}^2 + \tau_{2,n}^2}{\tau_{1,n}\tau_{2,n}^2}\sin\left(\frac{\tau}{\tau_{1,n}}\right)e^{-\tau/\tau_{2,n}}, \quad (7)
$$

where $\Theta(\tau)$ is the Heaviside step function [9]. f_n is the fractional contribution of the nth resonance to the overall Raman response function. The sum is performed over the N resonances of the material, each of which has its own characteristic response times τ_1 and τ_2. For LN we model $R(\tau)$ using $N = 4$ resonances with $\tau_1 = [21, 19.3, 15.9, 8.3]\,\text{fs}/t_0$, $\tau_2 = [544, 1021, 1361, 544]\,\text{fs}/t_0$, and $f_n = [0.635, 0.105, 0.02, 0.24]$ [20]. In silica $R(\tau)$ is typically modeled with $N = 1$ resonances with $\tau_1 = 12.2\,\text{fs}/t_0$, $\tau_2 = 32\,\text{fs}/t_0$, and $f_n = 1$ [23]. The resulting Raman responses of both LN and silica are plotted in Fig. 1 in the frequency domain.

III. TWO-COMPONENT SOLITONS

First, we analyze Eq. (2) without Raman terms ($\varepsilon_f = \varepsilon_s = 0$). Looking for soliton solutions ψ_f and ψ_s, we use the ansatz

$$
U_f = \psi_f(\eta, \mu, \nu)e^{i\mu\xi},
$$
$$
U_s = \psi_s(\eta, \mu, \nu)e^{i[2\mu-\kappa]\xi}. \quad (8)
$$

where $\eta = \tau - \nu\xi$, μ is the nonlinear shift to the propagation constant, and ν is the inverse soliton velocity. These two soliton parameters can be chosen freely; however, the relative

values of μ and ν are restricted by the criteria

$$4r_2\mu > \nu^2,$$

$$4s_2[2\mu - \kappa] > [\nu - s_1]^2, \qquad (9)$$

which ensure exponential localization in the FF and SH components, respectively [15]. These existence criteria can be visualized in the ν-μ plane as the areas above (below) two parabolas, in the case of anomalous (normal) dispersion, $r_2 = 1$, $s_2 > 0$ ($r_2 = -1$, $s_2 < 0$). Both criteria must be satisfied for solitons to exist, which occurs in the region where the two parabolic areas overlap.

Substitution of our ansatz in Eq. (8) into Eq. (2) results in

$$\hat{S}\vec{X} = 0, \qquad (10)$$

which we have written in matrix form for convenience:

$$\hat{S} = \begin{bmatrix} A & C^* & B & 0 \\ C & D & 0 & 0 \\ B^* & 0 & A^* & C \\ 0 & 0 & C^* & D^* \end{bmatrix}, \quad \vec{X} = \begin{bmatrix} \psi_f \\ \psi_s \\ \psi_f^* \\ \psi_s^* \end{bmatrix}, \qquad (11)$$

with matrix elements

$A = -\mu - i\nu\partial_\eta + r_2\partial_\eta^2 + \alpha_f|\psi_f|^2 + \alpha_c|\psi_s|^2,$

$B = \psi_s/2,$

$C = \psi_f/2,$

$D = -2\mu + \kappa + i[s_1 - \nu]\partial_\eta + s_2\partial_\eta^2 + \alpha_s|\psi_s|^2 + \alpha_c|\psi_f|^2.$

$\qquad\qquad\qquad\qquad\qquad\qquad\qquad (12)$

Previous work has identified soliton solutions in this system of equations [16,18]. Importantly, localized soliton solutions are possible when the signs of dispersion in the FF and SH are the same [15]. We note two results of particular relevance for this work on bright temporal solitons. First, in the case of anomalous dispersion many families of soliton solutions exist with only one, known as "C type," being stable [18]. Second, in the case of normal dispersion where $\chi^{(3)}$ and $\chi^{(2)}$ nonlinearities are in opposition, only one family of solitons exists, below a certain peak power [18]. In both cases these solitons are nonzero in both the FF and SH components, which in this work we refer to as two-component solitons.

For these two-component solitons there are three regimes worth noting here. The first is the Kerr limit when $\chi^{(3)}$ nonlinearity dominates ($\psi_f|\psi_f|^2\alpha_f \gg \psi_f^*\psi_s$) and the majority of the soliton power resides in the FF component. The second is the cascaded Kerr limit where $\chi^{(2)}$ nonlinearity is dominant ($\psi_f|\psi_f|^2\alpha_f \ll \psi_f^*\psi_s$ and $\psi_f|\psi_f|^2\alpha_c \ll \psi_f^2$) and phase mismatch is large, $|\kappa| \gg |\mu|$, with the correct sign such that $\kappa r_2 < 0$. In this regime the interaction between the SH and FF can be approximated as a cascaded Kerr term in the FF, giving rise to solitons similar in form to those in the true Kerr limit and with a negligible SH component [16]. The last is the quadratic limit, where $\chi^{(2)}$ nonlinearity is dominant and phase mismatch is small. This regime is characterized by a more even distribution of power between the FF and SH, and neither component is negligible.

We find two-component soliton solutions to Eq. (10) using the Newton-Raphson method with the known analytic quadratic soliton solution as the initial condition [16]. Taking the Fourier transform of these solutions, we then find
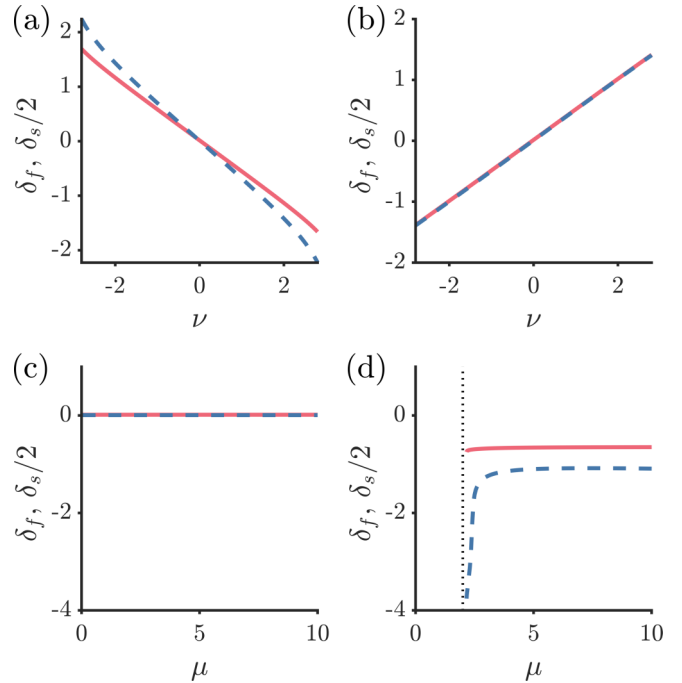

FIG. 2. Frequency shift of soliton components as a function of ν and μ, calculated by the numerical Newton-Raphson method. δ_f and $\delta_s/2$ are plotted by solid red and dashed blue lines, respectively. Panels are representative of solitons in the (a) quadratic limit with anomalous dispersion ($\mu = 5$, $\kappa = 0$, $s_1 = 0$, $r_2 = 1$, $s_2 = 1/4$) and (b) Kerr limit with normal dispersion ($\mu = -2$, $\kappa = 300$, $s_1 = 0$, $r_2 = -1$, $s_2 = -1/4$). (c) and (d) show data for solitons in the quadratic limit with anomalous dispersion ($\kappa = 0$, $s_1 = 0$, $r_2 = 1$, $s_2 = 1/16$). Inverse soliton velocity $\nu = 0$ and $\nu = 1$ in (c) and (d), respectively. The black dotted line marks the boundary of soliton existence for the given ν found using Eq. (9) [$\mu = 0$ and $\mu = 2$ in (c) and (d), respectively]. $t_0 = 100$ fs throughout.

the frequency of the spectral peaks ω_f' and ω_s' of the FF and SH components, respectively. We define the normalized frequency shift of each component from their reference frequencies as $\delta_f = [\omega_f' - \omega_f]t_0$ for the FF and, similarly, δ_s for the SH component. We note that these definitions place no constraint on the shift of the SH relative to the FF; therefore, the peak frequency of the SH component may not necessarily be twice that of the FF, as shown in Fig. 2(a).

In Fig. 2(a) we plot δ_f and $\delta_s/2$ as a function of inverse soliton velocity ν. Only where the two plotted functions coincide is the peak frequency of the SH component exactly double that of the FF. There is a clear difference between the quadratic and Kerr limits illustrated in Figs. 2(a) and 2(b), respectively. Considering the relative powers in each component for each regime, this difference can be easily understood. In the Kerr limit the majority of the soliton power resides in the FF component, and so behavior of the SH is dominated by its interaction with the FF; thus, δ_s is locked at exactly twice δ_f. Conversely, in the quadratic regime where the power is more evenly shared between both components, we see the spectral shifts are not dominated by a single component. The different signs of dispersion in Figs. 2(a) and 2(b) govern the sign of the gradient of δ_f and δ_s.

Figures 2(c) and 2(d) plot δ_f and $\delta_s/2$ as a function of the soliton parameter μ. The difference between these two panels is the inverse soliton velocity ν. The importance of this difference becomes clear when we consider the soliton existence criteria in Eq. (9). Looking first at Fig. 2(c), where $\nu = 0$, we notice that $\delta_f = \delta_s/2 = 0$ for the range of μ shown. In Fig. 2(d), however, where $\nu = 1$, the behavior is not as simple. For large μ values we see that $\delta_f \neq \delta_s/2$, which is expected from Fig. 2(a). For smaller μ values, however, we see that δ_s shifts rapidly as μ approaches the boundary of soliton existence without much change in δ_f. Unlike in Kerr solitons there is no simple relationship between shifts in ν and μ and the spectral shifts in two-component solitons. It is a complicated dependence reflecting the balance of power between and dispersion of each component.

IV. RAMAN SHIFT

Now we consider the effects of a small, but nonzero, Raman response ($\varepsilon_f = \varepsilon_s \neq 0$). To accommodate this change our ansatz in Eq. (8) becomes

$$
\begin{aligned}
U_f &= [\psi_f(\eta, \mu, \nu) + a_f(\xi, \eta)]e^{i\phi}, \\
U_s &= [\psi_s(\eta, \mu, \nu) + a_s(\xi, \eta)]e^{i2\phi - i\kappa\xi},
\end{aligned}
\tag{13}
$$

where we now allow μ and ν to slowly vary with ξ. Our transverse coordinate, $\eta = \tau - \int \nu d\xi$, keeps pace with the soliton as its inverse velocity ν changes. $\phi = \int \mu d\xi$, allowing for the phase of the soliton to evolve as the propagation constant μ changes with ξ. We introduce the small terms $a_f \ll \psi_f$ and $a_s \ll \psi_s$ to allow for corrections to the soliton profile and radiation from the solitons. Now the soliton parameters ν and μ can vary; we expect that the position of the soliton will move on the ν-μ plane where without Raman terms the soliton was previously a static point. The trajectory that the soliton takes and how it interacts with the existence criteria in Eq. (9) will be discussed in Sec. VI.

Using our ansatz (13), we derive (see the Appendix) shifts in the soliton parameters

$$
\dot{\nu} = \frac{\partial \nu}{\partial \xi} = F_\nu(\tilde{\varepsilon}_f, \tilde{\varepsilon}_s, \psi_f, \psi_s, \nu, \mu),
$$

$$
\dot{\mu} = \frac{\partial \mu}{\partial \xi} = F_\mu(\tilde{\varepsilon}_f, \tilde{\varepsilon}_s, \psi_f, \psi_s, \nu, \mu).
\tag{14}
$$

These equations (the forms of F_ν and F_μ are given in the Appendix) can then be integrated to find $\nu(\xi)$ and $\mu(\xi)$.

Once $\nu(\xi)$ and $\mu(\xi)$ are known, we can then calculate the temporal shift of the soliton,

$$
\tau_s(\xi) = \int_0^\xi \nu(\xi')d\xi',
\tag{15}
$$

and the shift in the peak frequency of each soliton component,

$$
\dot{\delta}_k = \frac{\partial \delta_k}{\partial \xi} = [\partial_\nu \delta_k]\dot{\nu} + [\partial_\mu \delta_k]\dot{\mu},
\tag{16}
$$

where k is either f or s for the FF or SH, respectively. Both $\partial_\nu \delta_k$ and $\partial_\mu \delta_k$ can, in general, be computed numerically for each soliton component, as described in Sec. III. These time and frequency shifts allow a simple comparison with simulated pulse propagation (see Sec. V).

Kerr limit

It is useful to consider the Kerr limit and observe how our results in Eqs. (14) and (16) converge to the well-known results for pure Kerr solitons. In the Kerr limit we neglect U_s and require anomalous dispersion ($r_2 = 1$). With these changes our model in Eq. (2) becomes the nonlinear Schrödinger equation (NLS),

$$
i\partial_\xi U_f + \partial_\tau^2 U_f + \alpha_f U_f |U_f|^2 = \varepsilon_f(U_f, 0),
\tag{17}
$$

which is invariant under the Galilean transform [24]

$$
U_f \to U_f \exp\left(i\frac{\nu}{2}\eta + i\frac{\nu^2}{4}\xi\right),
$$

$$
\tau \to \tau - \nu\xi = \eta.
\tag{18}
$$

The NLS has known solutions for solitons of velocity ν [24],

$$
U_f(\eta) = \psi_0 \exp\left(i\mu\xi + i\frac{\nu}{2}\eta\right),
\tag{19}
$$

where we have defined the real soliton profile [1],

$$
\psi_0 = \sqrt{\frac{2q}{\alpha_f}}\operatorname{sech}(\sqrt{q}\eta),
\tag{20}
$$

where $q = \mu - \nu^2/4$. From our previous ansatz, Eq. (8), we can see that $\psi_f = \psi_0 \exp(i\nu\eta/2)$, and we neglect ψ_s terms. We then use the approximate, small-bandwidth form of the Raman response in silica $\tilde{\varepsilon}_f = \psi_f \tau_R \partial_\eta[\alpha_f|\psi_f|^2]$, where $\tau_R = f_R \int \tau R(\tau)d\tau = 0.0073$ [25]. Using these substitutions and integrating Eq. (14) [the full functional form is given by Eq. (A7)], we restore the known result for the Kerr limit in silica [1,8],

$$
\dot{\nu} = \frac{32}{15}\tau_R q^2,
\tag{21}
$$

where we have used the integrals

$$
\int_{-\infty}^{\infty} x\operatorname{sech}^2(x)\tanh(x)dx = 1,
$$

$$
\int_{-\infty}^{\infty} \operatorname{sech}^4(x)\tanh^2(x)dx = \frac{4}{15}.
\tag{22}
$$

Similarly, one can find that

$$
\dot{\mu} = \frac{\nu}{2}\dot{\nu}
\tag{23}
$$

and therefore restore

$$
\mu(\xi) = q + \frac{[\nu(\xi)]^2}{4},
\tag{24}
$$

as expected from the Galilean transform in Eq. (18).

From Eq. (18) we know that a change in inverse soliton velocity ν results in a subsequent change in the soliton frequency $\delta_f = -\nu/2$. Using this, we can find the rate of frequency shift,

$$
\dot{\delta}_f = [\partial_\nu \delta_f]\dot{\nu} = -\frac{16}{15}\tau_R q^2,
\tag{25}
$$

which also agrees with known results for the Kerr limit in silica [1,8].

For the general case, where the Raman response is not simply linear over the bandwidth of the soliton (as in LN) or where the SH component is significant, the Raman shifts can
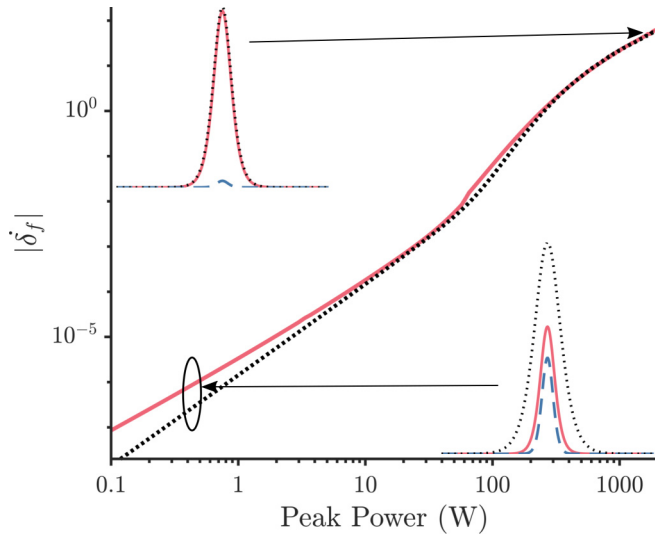
FIG. 3. Rate of frequency shift $\dot{\delta}_f$ predicted by Eq. (16) for two-component solitons and Kerr solitons in LN nanowaveguides, shown as solid red and dotted black curves, respectively (for $\nu = 0$). For the two-component solitons we plot the peak power as $|A_f|^2 + |A_s|^2$. Insets compare soliton power profiles at high and low powers. FF and SH of the two-component solitons are plotted as solid red and dashed blue curves, respectively. The Kerr soliton power profile is shown as a dotted black curve with the same total peak power. We found that $\dot{\delta}_s/2$ very closely followed the same trend as $\dot{\delta}_f$ for the two-component soliton in this case.

be calculated numerically. Doing this for LN, we find that in the Kerr limit the FF component of the two-component soliton shifts in frequency at the same rate as a Kerr soliton of the same peak power. In the quadratic limit, when the soliton has a significant SH component, we find that the FF frequency shift differs significantly from that expected for a Kerr soliton of the same peak power. This trend is illustrated in Fig. 3. We compare solitons of the same peak power as Eq. (25) shows us the simple relationship between $\dot{\delta}_f$ and q [which from Eq. (20) is proportional to soliton peak power] in the Kerr limit.

V. SIMULATIONS

In order to assess their validity outside of the Kerr limit and linear Raman response regime, we compare our predictions in Eqs. (15) and (16) with numerical simulations of Eq. (2) using the split-step Fourier method. We use numerical soliton solutions as the initial inputs for both the simulations and predictions. In these comparisons we chose dispersion and soliton parameters that are feasible in LN nanowaveguides at reasonable input powers.

We present four typical examples of such comparisons in Fig. 4 which are representative of two soliton limits each in two dispersion regimes. In two of these examples dispersion is anomalous, and phase mismatches of $\kappa = 0$ and $\kappa = 300$ provide quadratic and cascaded Kerr limits, respectively. The other two examples explore the normal dispersion regime again with quadratic and cascaded Kerr limits represented. We ensure the Raman term is a perturbation to the soliton equation by operating in the quadratic and cascaded Kerr regimes. This keeps all Kerr terms, including Raman, relatively small. We

also used an initial inverse soliton velocity $\nu = 0$ such that the input pulse was not shifted from the reference frequencies initially (i.e., $\delta_f = \delta_s = 0$ at $\xi = 0$).

Figures 4(a) and 4(b) show remarkable similarity between prediction and simulation for Raman-shifting quadratic two-component solitons under anomalous and normal dispersion, respectively. These examples are particularly important as they validate our predictions outside of the Kerr limit, in regimes where the SH soliton component is similar in power to that of the FF. In Figs. 4(c) and 4(d) the phase mismatch κ is set such that the solitons are in the cascaded Kerr regime with very small SH components. In these examples we see qualitative agreement between our predictions and simulations. The reason some predictions do not match the simulations more closely is largely down to the spectral cutoff of the soliton due to the sharp Raman peak in LN [9]. The sharp Raman peaks in LN are clear when compared with silica in Fig. 1. This has been seen before in solitons in air-core fibers where a significant portion of the initial pulse propagates as nonsolitonic radiation [9]. The soliton propagating in the simulation is therefore not necessarily the same as the input soliton for which the predictions are made.

We point out that although the Raman frequency shift is always towards lower frequencies as expected, the temporal shift of the soliton is dependent on the sign of dispersion. Under anomalous dispersion lower frequencies travel slower, and so as the soliton shifts to lower frequencies, it slows, moving in the positive time direction (arriving late). Under normal dispersion the opposite is true (and the soliton arrives early).

VI. SOLITON INSTABILITIES

We now consider the soliton trajectory in the ν-μ plane, predicted by Eq. (14), in relation to the soliton existence criteria given in Eq. (9). Doing so prompts us to ask two questions: does the trajectory of the soliton approach the boundary of soliton existence, and if so, what happens to the soliton when it does?

Considering Kerr solitons, only one existence criterion is relevant, which is similar to that of the FF with anomalous dispersion ($r_2 = 1$). The criterion for soliton existence is therefore $4\mu > \nu^2$. We note that Kerr solitons follow the trajectory described by Eq. (24), which we notice is always tangential to the existence boundary, $\mu = \nu^2/4$. This is not a coincidence and is due to the simple relation between the shift in soliton frequency and inverse velocity ν given by the Galilean transform in Eq. (18). A Raman-shifting Kerr soliton therefore does not approach the boundary of soliton existence.

In the case of two-component solitons, however, the relation between frequency and inverse velocity shifts is not simple. There are also two existence criteria that must both be satisfied and which, in general, do not coincide. It is therefore unclear whether a Raman-shifting two-component soliton will approach the boundary of soliton existence.

Here, we give two examples that demonstrate that two-component solitons can approach the boundary of existence. In these examples we use systems where the group-velocity dispersion in one component is significantly smaller than that in the other (e.g., $s_2 \ll r_2$). These parameters are chosen as a simple means of narrowing the region of soliton
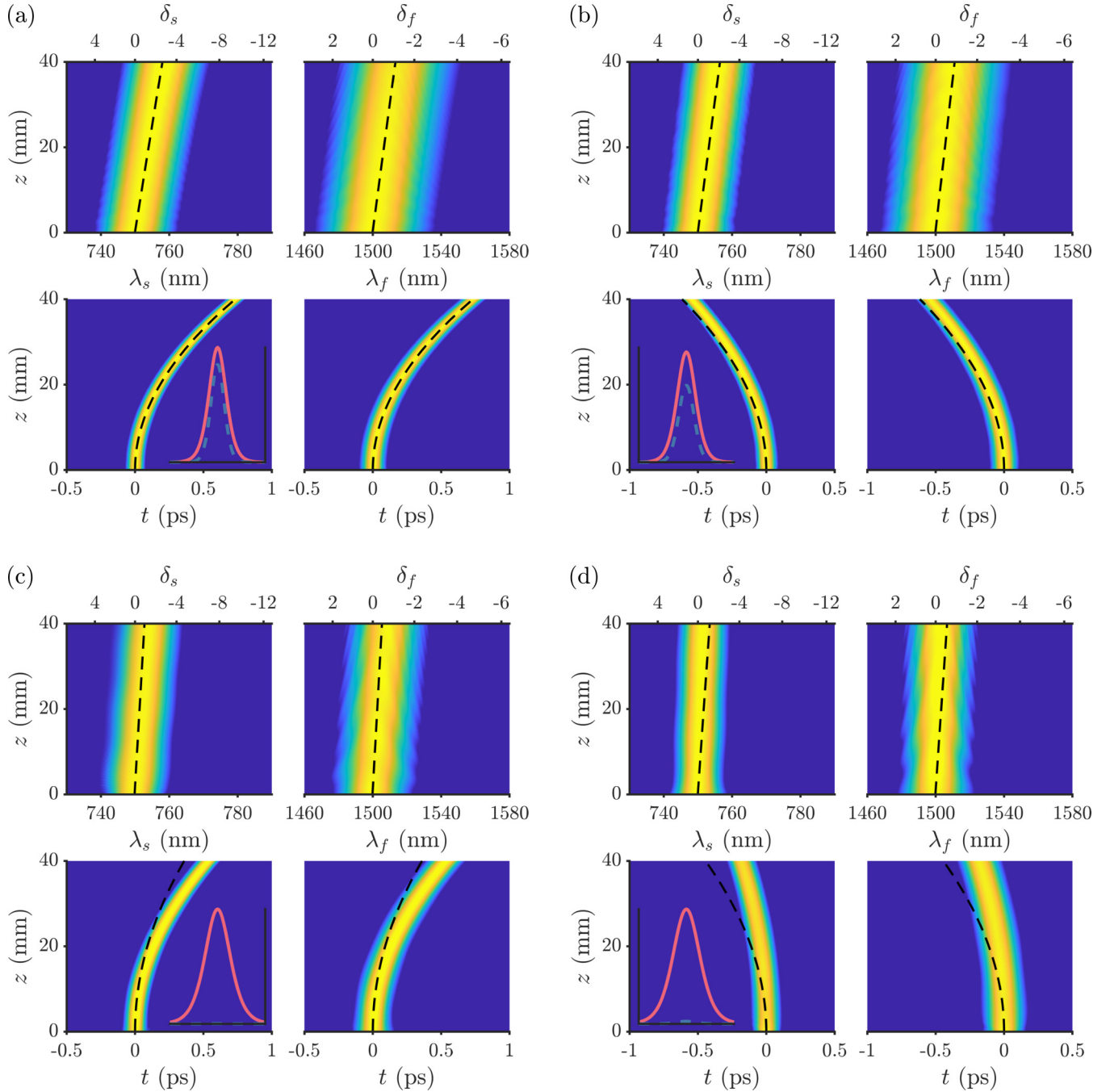
FIG. 4. Simulated soliton propagation in time and frequency domains shown in the top and bottom plots in each panel, respectively. The FF and SH are shown on the right and left sides of each panel, respectively. Dashed lines show time and frequency shifts predicted by Eqs. (15) and (16). Insets show the relative input soliton power plotted in the time domain for FF (solid red) and SH (dashed blue). (a) and (b) show solitons in the quadratic limit with anomalous and normal dispersion, respectively. (c) and (d) show solitons in the cascaded Kerr limit with anomalous and normal dispersion, respectively. Parameters used in each panel are as follows: (a) $\mu = 5$, $\nu = 0$, $\kappa = 0$, $s_1 = 0$, $r_2 = 1$, $s_2 = 1/4$. (b) $\mu = -5$, $\nu = 0$, $\kappa = 0$, $s_1 = 0$, $r_2 = -1$, $s_2 = -1/4$. (c) $\mu = 2$, $\nu = 0$, $\kappa = -1000$, $s_1 = 10$, $r_2 = 1$, $s_2 = 1/4$. (d) $\mu = -2$, $\nu = 0$, $\kappa = 300$, $s_1 = 0$, $r_2 = -1$, $s_2 = -1/4$. For all of these simulations we used an input FF wavelength of 1500 nm ($\omega_f/2\pi = 200$ THz), characteristic timescale $t_0 = 100$ fs, and $\alpha_f = 0.0007$, $\alpha_s = 0.008$, $\alpha_c = 0.005$.

existence, as shown in Figs. 5(a) and 5(d), thus reducing the shift required to approach the existence boundary. Tracking the soliton as it shifts in μ and ν, we find that, initially, the soliton shifts parallel to the FF localization boundary and therefore approaches the boundary existence, which in these cases is the boundary of SH localization. Close to this boundary we find our predictions in Eq. (14) break down as the calculation of updated soliton solutions becomes more difficult. After this we rely on our simulations to see what happens.
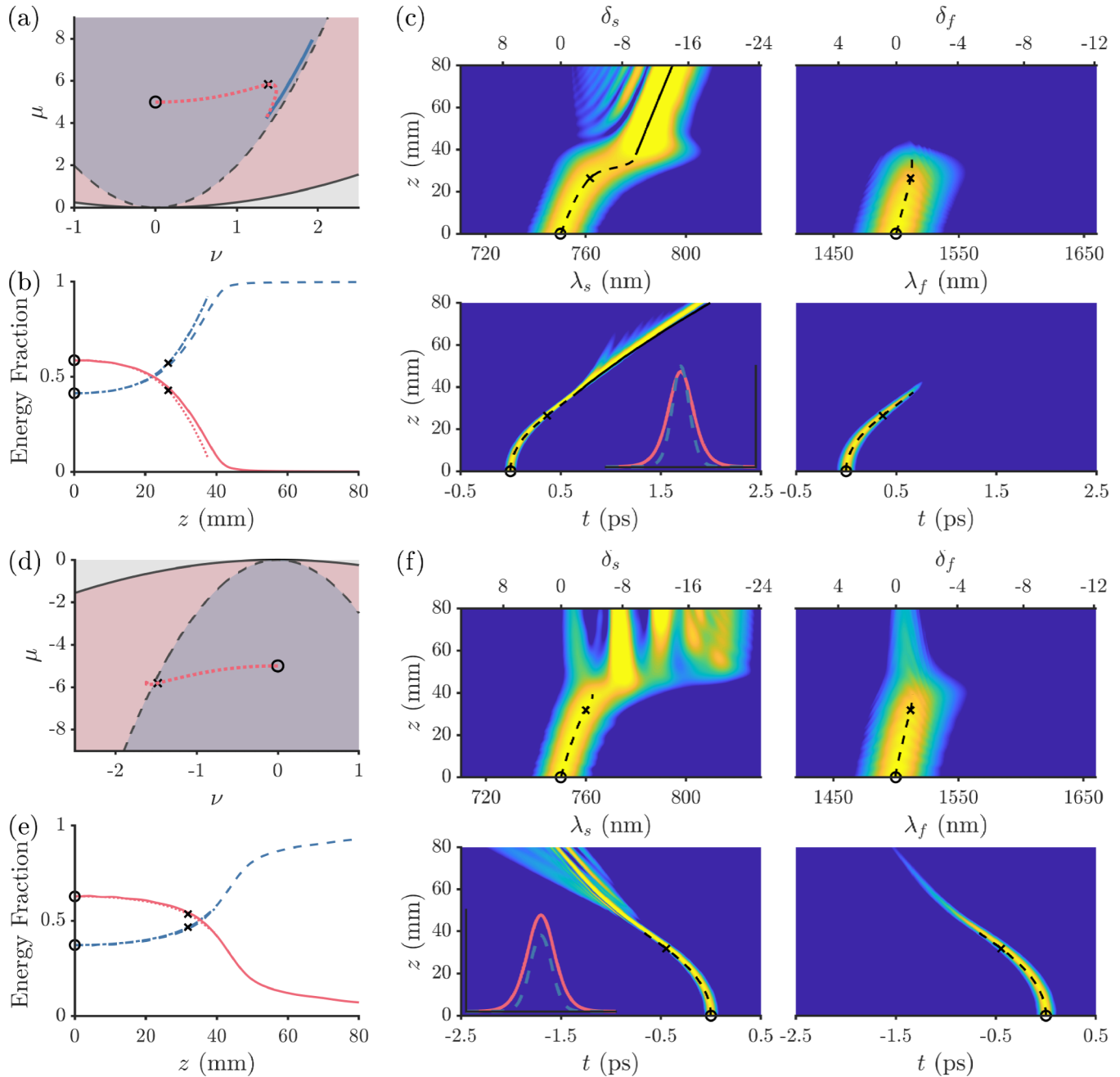
FIG. 5. Prediction and simulation of soliton instabilities. (a)–(c) show an example under anomalous dispersion with the same parameters as in Fig. 4(a) except with $s_2 = 1/16$. (d)–(f) show an example under normal dispersion with parameters as in Fig. 4(b) but with $s_2 = -1/20$. Soliton existence analysis is shown in (a) and (d); shaded regions mark where each soliton existence criterion is met. The two-component soliton trajectory in the ν-μ plane predicted by Eq. (14) is included as the dotted red curve. The solid blue curve in (a) shows the predicted trajectory of the Kerr soliton in the SH after the two-component soliton becomes unstable. (b) and (e) plot the fractional energy in each component of the soliton as a function of propagation distance. Data from the simulated soliton propagation are plotted as solid red and dashed blue curves for the FF and SH, respectively. Fractional energies predicted by our analysis for the FF and SH are shown as dotted red and dot-dashed blue lines, respectively, calculated from numerical solitons for the predicted ν and μ values. (c) and (f) plot the simulated propagation of the solitons in each example. The top and bottom rows of each panel show the spectral and temporal evolution, respectively; the SH and FF are shown in the left and right columns, respectively. The trajectories of the soliton predicted by Eqs. (16) and (15) are plotted as dashed black curves in the spectral and temporal plots, respectively. Solid black curves in (c) plot predictions for a Kerr soliton in the SH after the two-component soliton becomes unstable. Insets plot relative input soliton power in the time domain for the FF (solid red curve) and SH (dashed blue curve). Circles mark the initial soliton position; crosses mark a particular point of interest in (a)–(c) and (d)–(f).

In the example in Figs. 5(a)–5(c), dispersion is anomalous, and we find that the soliton appears to recoil [6] to avoid the existence boundary, as shown in Fig. 5(a). At the point marked with a cross in Figs. 5(a)–5(c) the soliton abruptly changes trajectory, shifting down in μ and very little in ν, still approaching the existence boundary. In Fig. 5(c) we see that this recoil in the ν-μ plane is accompanied by a rapid frequency shift of the SH component, shown in the simulated spectrum and replicated remarkably closely by our predictions. We note that this frequency shift is similar to that shown in Fig. 3(d), where δ_s rapidly shifts as μ decreases and the soliton approaches the existence boundary. In this example we see the majority of the soliton energy is transferred to the SH, as shown clearly in Fig. 5(b), where again our predictions closely follow the initial stages of the simulation. After the two-component soliton is destabilized, a purely Kerr soliton appears to form in the SH with minimal energy in the FF component. Comparing the predicted spectral and temporal shifts for a SH Kerr soliton of the same peak power with the simulations in Fig. 5(c), we see they match very closely. In Fig. 5(a) we plot the trajectory on the ν-μ plane predicted for this Kerr soliton, which we find is tangential to the boundary of existence, as expected. We therefore conclude that the outcome of the two-component soliton instability is the birth of a Kerr soliton in the SH.

Under normal dispersion the soliton initially behaves similarly, shifting towards the boundary of SH existence, as shown in Fig. 5(d). In this case, however, we do not see any recoil of the soliton in the ν-μ plane at the position marked by the cross. As there is no recoil in the ν-μ plane, we predict no rapid spectral shift. This is confirmed by simulations in Fig. 5(f), where the rapid frequency shift seen in the SH occurs well after our predictions stop and therefore after the soliton has shifted out of its region of existence. Once again, we see a large transfer of energy from the FF to the SH, which is presented in Fig. 5(e), although not as complete as in the anomalous dispersion case. We can see from the simulation in Fig. 5(f) that the SH and remaining FF components disperse after the instability, producing a broad spectrum in the SH. We do not expect a Kerr soliton in the SH, as this is not possible under normal dispersion.

We have also run predictions and simulations of systems where $r_2 \ll s_2$ and found similar results. The major difference in these cases is that the power is transferred to the FF rather than the SH during the instability development.

VII. CONCLUSION

In this work we have developed a theory of Raman-induced self-frequency shift in two-component solitons accounting for both $\chi^{(2)}$ and $\chi^{(3)}$ nonlinearities. Our analysis predicts the acceleration and accompanying frequency shift of each soliton component. Expressions for the temporal and propagation constant shifts have also been presented. Known results for purely Kerr solitons have been reproduced by analyzing two-component solitons in the Kerr limit, and we showed how our results differ outside this limit. Our predictions were validated by comparison with numerical simulation of soliton propagation in LN nanowaveguides which show good qual-

itative agreement in every case and remarkable quantitative agreement in some cases.

We have proposed that two-component Raman solitons may approach the boundary of their own existence, which we showed does not happen in Kerr solitons. We have described a few scenarios of the unstable dynamics of the two-component solitons induced by the Raman effect shifting the soliton frequency towards the boundary of its existence. Our theory predicts the initial stage of this process and matches remarkably closely with simulations.

The predictions made here can be applied to future work on ultrashort pulses in systems with $\chi^{(2)}$ and $\chi^{(3)}$ nonlinearity, including not only the focus of this work, temporal solitons in waveguides, but also multidimensional solitons in bulk media [26]. These results also show the potential of these systems to produce novel soliton dynamics. In particular, the theory of two-component Raman solitons may prove useful in the engineering and understanding of new sources of supercontinuum generation and frequency conversion.

All data supporting this study are openly available from the University of Bath Research Data Archive [27].

APPENDIX: RAMAN SHIFT THEORY

Substituting our ansatz for a Raman-shifting soliton, Eq. (13), into our model, Eq. (2), our governing equation becomes

$$\hat{S}\vec{X} + \hat{P}\vec{X} + \hat{J}\vec{a} = \vec{\varepsilon}, \tag{A1}$$

where $\hat{S}$ and $\vec{X}$ are defined as before and

$$\hat{P} = i\begin{bmatrix} G & 0 & 0 & 0 \\ 0 & G & 0 & 0 \\ 0 & 0 & -G^* & 0 \\ 0 & 0 & 0 & -G^* \end{bmatrix}, \quad \vec{a} = \begin{bmatrix} a_f \\ a_s \\ a_f^* \\ a_s^* \end{bmatrix},$$

$$\hat{J} = \begin{bmatrix} M & N & Q & R \\ N^* & T & R & W \\ Q^* & R^* & M^* & N^* \\ R^* & W^* & N & T^* \end{bmatrix}, \quad \vec{\varepsilon} = \begin{bmatrix} \tilde{\varepsilon}_f \\ \tilde{\varepsilon}_s \\ \tilde{\varepsilon}_f^* \\ \tilde{\varepsilon}_s^* \end{bmatrix}, \tag{A2}$$

with the matrix elements

$$G = [\partial_\xi \mu]\partial_\mu + [\partial_\xi \nu]\partial_\nu,$$

$$M = -\mu - i\nu\partial_\eta + r_2\partial_\eta^2 + 2\alpha_f|\psi_f|^2 + \alpha_c|\psi_s|^2,$$

$$N = \psi_f^* + \alpha_c\psi_s^*\psi_f,$$

$$Q = \psi_s + \alpha_f\psi_f^2,$$

$$R = \alpha_c\psi_s\psi_f,$$

$$T = -[2\mu - \kappa] + i[s_1 - \nu]\partial_\eta + s_2\partial_\eta^2 + 2\alpha_s|\psi_s|^2 + \alpha_c|\psi_f|^2,$$

$$W = \alpha_s\psi_s^2. \tag{A3}$$

We have kept terms up to the order of $\vec{a}$; smaller terms have been neglected. As $\vec{\varepsilon}$ is also a small quantity, terms proportional to $\vec{\varepsilon}\vec{a}$ are very small and so are neglected. We also introduce the notation $\tilde{\varepsilon}_f = \varepsilon_f(\psi_f, \psi_s)$ and $\tilde{\varepsilon}_s = \varepsilon_s(\psi_f, \psi_s)$.

Recognizing from before that $\hat{S}\vec{X} = 0$, we reduce the left-hand side in Eq. (A1) to two terms. To make further progress we project Eq. (A1) onto the zero eigenvectors of $\hat{J}^\dagger = \hat{J}$ (as $\hat{J}$ is self-adjoint). So Eq. (A1) becomes

$$(\vec{v}_n, \hat{P}\vec{X}) + (\vec{v}_n, \hat{J}\vec{a}) = (\vec{v}_n, \vec{\tilde{\varepsilon}}), \tag{A4}$$

where the term $\hat{J}\vec{a}$ vanishes by construction. n is either 1 or 2, such that $\vec{v}_n$ is one of the two zero eigenvectors of $\hat{J}$,

$$\vec{v}_1 = \partial_\eta \vec{X}, \qquad \vec{v}_2 = \begin{bmatrix} \psi_f \\ 2\psi_s \\ -\psi_f^* \\ -2\psi_s^* \end{bmatrix}. \tag{A5}$$

The results of projecting Eq. (A1) onto $\vec{v}_1$ and $\vec{v}_2$ are, respectively,

$$\begin{aligned} \mathrm{Im} \int_{-\infty}^{\infty} [\partial_\eta \psi_f^*][G\psi_f] &+ [\partial_\eta \psi_s^*][G\psi_s]\,d\eta \\ &= -\mathrm{Re} \int_{-\infty}^{\infty} [\partial_\eta \psi_f^*]\tilde{\varepsilon}_f + [\partial_\eta \psi_s^*]\tilde{\varepsilon}_s\,d\eta, \\ \mathrm{Re} \int_{-\infty}^{\infty} \psi_f^*[G\psi_f] &+ 2\psi_s^*[G\psi_s]\,d\eta \\ &= \mathrm{Im} \int_{-\infty}^{\infty} \psi_f^*\tilde{\varepsilon}_f + 2\psi_s^*\tilde{\varepsilon}_s\,d\eta. \end{aligned} \tag{A6}$$

Using these two equations, we find the shift of our two soliton parameters μ and ν to be

$$\begin{aligned} \dot{\nu} = \frac{\partial \nu}{\partial \xi} &= \frac{C_2 A_1 - C_1 A_2}{B_2 A_1 - B_1 A_2}, \\ \dot{\mu} = \frac{\partial \mu}{\partial \xi} &= \frac{C_1 B_2 - C_2 B_1}{B_2 A_1 - B_1 A_2}, \end{aligned} \tag{A7}$$

where we introduce the parameters

$$\begin{aligned} A_1 &= \mathrm{Im} \int_{-\infty}^{\infty} [\partial_\eta \psi_f^*][\partial_\mu \psi_f] + [\partial_\eta \psi_s^*][\partial_\mu \psi_s]\,d\eta, \\ B_1 &= \mathrm{Im} \int_{-\infty}^{\infty} [\partial_\eta \psi_f^*][\partial_\nu \psi_f] + [\partial_\eta \psi_s^*][\partial_\nu \psi_s]\,d\eta, \\ C_1 &= \mathrm{Im} \int_{-\infty}^{\infty} [\partial_\eta \psi_f^*]\tilde{\varepsilon}_f + [\partial_\eta \psi_s^*]\tilde{\varepsilon}_s\,d\eta, \\ A_2 &= \mathrm{Re} \int_{-\infty}^{\infty} \psi_f^*[\partial_\mu \psi_f] + 2\psi_s^*[\partial_\mu \psi_s]\,d\eta, \\ B_2 &= \mathrm{Re} \int_{-\infty}^{\infty} \psi_f^*[\partial_\nu \psi_f] + 2\psi_s^*[\partial_\nu \psi_s]\,d\eta, \\ C_2 &= \mathrm{Re} \int_{-\infty}^{\infty} \psi_f^*\tilde{\varepsilon}_f + 2\psi_s^*\tilde{\varepsilon}_s\,d\eta. \end{aligned} \tag{A8}$$

We point out that these parameters are themselves all μ and ν dependent through ψ_f and ψ_s. From Eq. (A7) we integrate over ξ using numerical soliton profiles $\psi_f(\mu, \nu)$ and $\psi_s(\mu, \nu)$ to find the inverse soliton velocity $\nu(\xi)$ and the soliton propagation constant $\mu(\xi)$. As a result of the ν and μ dependence of ψ_f and ψ_s, accurate calculation of these shifts requires repeated evaluation of Eq. (A7), with ψ_f and ψ_s being updated on each iteration for the current shifted μ and ν values.

[1] G. P. Agrawal, *Nonlinear Fiber Optics*, 5th ed, Optics and Photonics (Academic Press, Burlington, MA, 2013).

[2] Y. S. Kivshar, G. P. Agrawal, and G. P. Agrawal, in *Optical Solitons*, edited by Y. S. Kivshar, G. P. Agrawal, and G. P. Agrawal (Academic Press, Burlington, MA, 2003), pp. 63–103.

[3] J. M. Dudley and J. R. J. R. Taylor, *Supercontinuum Generation in Optical Fibers* (Cambridge University Press, Cambridge, 2010).

[4] J. P. Gordon, Opt. Lett. **11**, 662 (1986).

[5] Y. Kodama and A. Hasegawa, IEEE J. Quantum Electron. **23**, 510 (1987).

[6] D. V. Skryabin, F. Luan, J. C. Knight, and P. S. J. Russell, Science **301**, 1705 (2003).

[7] F. Biancalana, D. V. Skryabin, and A. V. Yulin, Phys. Rev. E **70**, 016615 (2004).

[8] D. V. Skryabin and A. V. Gorbach, in *Supercontinuum Generation in Optical Fibers*, edited by J. M. Dudley and J. R. Taylor (Cambridge University Press, Cambridge, 2010), pp. 178–198.

[9] A. V. Gorbach and D. V. Skryabin, Opt. Express **16**, 4858 (2008).

[10] H. Guo, B. Zhou, M. Steinert, F. Setzpfandt, T. Pertsch, H.-p. Chung, Y.-H. Chen, and M. Bache, Opt. Lett. **40**, 629 (2015).

[11] C. R. Phillips, C. Langrock, J. S. Pelc, M. M. Fejer, I. Hartl, and M. E. Fermann, Opt. Express **19**, 18754 (2011).

[12] H. Guo, X. Zeng, B. Zhou, and M. Bache, J. Opt. Soc. Am. B **30**, 494 (2013).

[13] G. Poberaj, H. Hu, W. Sohler, and P. Günter, Laser Photonics Rev. **6**, 488 (2012).

[14] A. Boes, B. Corcoran, L. Chang, J. Bowers, and A. Mitchell, Laser Photonics Rev. **12**, 1700256 (2018).

[15] W. R. Rowe, D. V. Skryabin, and A. V. Gorbach, Phys. Rev. Res. **1**, 033146 (2019).

[16] A. V. Buryak, P. D. Trapani, D. V. Skryabin, and S. Trillo, Phys. Rep. **370**, 63 (2002).

[17] R. Schiek, J. Opt. Soc. Am. B **10**, 1848 (1993).

[18] A. V. Buryak, S. Trillo, and Y. S. Kivshar, Opt. Lett. **20**, 1961 (1995).

[19] O. Bang, J. Opt. Soc. Am. B **14**, 51 (1997).

[20] M. Bache and R. Schiek, arXiv:1211.1721.

[21] L. Cai, A. V. Gorbach, Y. Wang, H. Hu, and W. Ding, Sci. Rep. **8**, 12478 (2018).

[22] A. V. Gorbach and E. Ivanov, Phys. Rev. A **94**, 013811 (2016).

[23] A. V. Gorbach and D. V. Skryabin, Phys. Rev. A **76**, 053803 (2007).

[24] Y. S. Kivshar, G. P. Agrawal, and G. P. Agrawal, in *Optical Solitons*, edited by Y. S. Kivshar, G. P. Agrawal, and G. P. Agrawal (Academic Press, Burlington, MA, 2003), pp. 31–62.

[25] D. V. Skryabin and A. V. Yulin, Phys. Rev. E **72**, 016619 (2005).

[26] O. Bang, Y. S. Kivshar, and A. V. Buryak, Opt. Lett. **22**, 1680 (1997).

[27] The supporting data for this article are openly available from the University of Bath Data Archive, https://doi.org/10.15125/BATH-00808.